Materials Science & Engineering A 663 (2016) 116–125

Contents lists available at ScienceDirect

Materials Science & Engineering A

journal homepage: www.elsevier.com/locate/msea

Effect of heat treatment on AlSi10Mg alloy fabricated by selective laser melting: Microstructure evolution, mechanical properties and fracture mechanism

Wei Li, Shuai Li, Jie Liu, Ang Zhang, Yan Zhou, Qingsong Wei *, Chunze Yan *, Yusheng Shi

State key Laboratory of Materials Processing and Die & Mould Technology, School of Materials Science and Engineering, Huazhong University of Science and Technology, Wuhan 430074, China

ARTICLE INFO

Article history:
Received 17 November 2015
Received in revised form
16 March 2016
Accepted 18 March 2016
Available online 19 March 2016

Keywords:
AlSi10Mg
Selective laser melting (SLM)
Heat treatment
Microstructure
Mechanical properties

ABSTRACT

The present paper systematically investigated the influence of solution and artificial aging heat treatments on the microstructures and mechanical properties of SLM-produced AlSi10Mg alloy parts. Due to the high cooling rate of SLM, an ultrafine eutectic microstructure in the as-built samples is characterized by spherical nano-sized network eutectic Si embedded in the Al matrix, which gives rise to significantly better tensile properties and Vickers micro-hardness. The solubility of Si atom in the Al matrix of as-built SLM samples is calculated to be 8.89 at%. With the increase in the solution temperature, the solubility decreases rapidly. The artificial aging causes the further decrease of the solubility of Si atoms in the Al matrix. Upon solution heat treatment, Si atoms are rejected from the supersaturated Al matrix to form small Si particles. With increasing the solution temperature, the size of the Si particles increases, whereas their number decreases. After artificial aging, the Si particles are further coarsened. The variation in size of Si particles has a significant influence on the mechanical properties of the AlSi10Mg samples. The tensile strength decreases from 434.25 ± 10.7 MPa for the as-built samples to 168.11 ± 2.4 MPa, while the fracture strain remarkably increases from 5.3 ± 0.22% to 23.7 ± 0.84% when the as-built sample is solution-treated at 550 °C for 2 h. This study indicates that the microstructure and mechanical properties of SLM-processed AlSi10Mg alloy can be tailored by suitable solution and artificial aging heat treatments.

1. Introduction

AlSi10Mg alloy, a hypoeutectic alloy in the Al-Si-Mg system, is highly demanded for many applications in aerospace, automotive industries and heat exchanger products [1], due to its light weight, low thermal expansion and recycling costs, and high mechanical properties [2]. It is well known that the morphology and size of eutectic silicon are the two most important factors significantly affecting the mechanical properties of AlSi10Mg alloy [3]. McDonald et al. [4] revealed that coarse and acicular eutectic silicon phases initiate cracks in the tension environment, which deteriorates mechanical properties. Therefore, it is imperative that the modification of coarse and acicular eutectic silicon phases is made to improve the mechanical properties of AlSi10Mg alloy for the ever-growing application demands in aerospace and other fields [5].

The modification of the eutectic silicon phase can be accomplished by rapid solidification [6–10]. Rapid solidification (10^6–10^8 °C/s) offers some distinct advantages such as the refinement of microstructure, the homogeneous distribution of eutectic silicon, the improvement of mechanical strength and ductility to meet the increasing demand for high performance of AlSi10Mg components [6,11]. However, it is not suitable for the majority of the casting processes as the cooling rate of most traditional casting processes is about 10^2 °C/s or less [6], and consequently the refinement of eutectic silicon has been greatly restricted. Although the cooling rate of melt spinning can reach 10^7 °C/s and nano-sized spherically shaped eutectic Si can be formed in some Al-Si-Mg alloys [12], the size and geometry of Al-Si-Mg components are severely constrained and only ribbons or small rods can be produced in the melt spinning process [5].

Selective laser melting (SLM), as a burgeoning metal additive manufacturing (AM) technology, is a powder bed fusion process, which is capable of realizing metal components with complex freeform geometries directly from three-dimensional (3D) computer aided design (CAD) data [13–15]. The laser energy is absorbed by powder particles complying with the complex coupling mechanisms between laser and materials, such as laser-bulk coupling and laser-powder coupling, when the high energy laser beam is radiated on powdered materials [16]. Due to the transient

* Corresponding authors.
E-mail addresses: wqs_xn@hust.edu.cn (Q. Wei), c_yan@hust.edu.cn (C. Yan).

http://dx.doi.org/10.1016/j.msea.2016.03.088
0921-5093/

interaction between the laser beam and the powder bed, a high temperature gradient (up to 10^5 °C/m) and a rapid cooling rate (up to 10^6–10^8 °C/s) occurs in the SLM process [17]. Therefore, the SLM process possessing extremely rapid solidification and a high cooling rate has great potential for the modification of the eutectic silicon phase in Al-Si-Mg alloys. The processing parameters of the SLM process have a substantial effect on the refinement of eutectic silicon and resultant mechanical properties of as-built AlSi10Mg components.

Recently, some efforts have been made to study the AlSi10Mg alloy fabricated by SLM. Yuan et al. [18] investigated the TiC/AlSi10Mg nanocomposites migration behavior and mechanism during SLM, and found that the particle size of TiC/AlSi10Mg varied from the standard nanoscale structure to the relatively coarsened submicron morphology with the increase of laser energy per unit length. Weingarten et al. [19] studied the physical mechanism of the hydrogen pores in AlSi10Mg parts built by SLM, and the hydrogen porosity could be lowered by the efficient drying of the powder as well as modification of the SLM process parameters. Qiu et al. [20] elaborated on the influence of processing conditions on strut structure and compressive properties of cellular lattice structures fabricated by selective laser melting. He discovered that the specific yield strength of AlSi10Mg is dependent of SLM processing conditions, indicating that further improvement in properties of AlSi10Mg can be achieved by process optimization. Read et al. [1] and Kempen et al. [21] focused their attentions on the optimization of SLM process parameters for building nearly fully dense AlSi10Mg parts. The as-built AlSi10Mg parts exhibit excellent mechanical properties like ultimate tensile strength owing to the very fine microstructure, but the elongation is relatively lower compared to the high pressure die cast counterparts.

Alloying magnesium to the Al-Si alloy enables the precipitation of Mg_2Si phase, which significantly improves ductility and strengthens the matrix without compromising other mechanical properties. AlSi10Mg can be hardened through the precipitation of Mg_2Si phase by a specified T^6 heat treatment (solution with complete artificial aging) [22]. Currently, there were some preliminary studies on the heat treatments of as-processed SLM AlSi10Mg parts. Brandl et al. [22] studied the microstructure, high cycle fatigue, and fracture behavior of as-built and peak-hardened treatment of SLM AlSi10Mg samples. They found that post heat treatment has the more considerable effect on the fatigue resistance of AlSi10Mg than building direction, and also the fatigue limit and static tensile strength significantly correlate with the size and morphology of eutectic silicon. Aboulkhair et al. [23] investigated the solution heat treatment and aging duration time on micro-hardness of SLM-processed AlSi10Mg. As far as the authors' knowledge, few work has systematically studied on the eutectic silicon evolution and mechanical properties of SLM-made AlSi10Mg parts when subjected to heat treatment.

Therefore, in the present paper, a systematically investigation has been conducted on the influence of solution and artificial aging on the eutectic microstructure and mechanical properties of SLM-produced AlSi10Mg alloy parts. Also, a possible transformation mechanism of this novel eutectic microstructure is proposed.

2. Experimental details

2.1. AlSi10Mg specimens fabricated by SLM

A gas atomized AlSi10Mg powder with a normally distribution from 20 μm to 63 μm was supplied by TLS Technik GmbH & Co Ltd. AlSi10Mg cubical samples of $15 \times 15 \times 15$ mm^3 and tensile bars shown in Fig. 1 were fabricated on a SLM250 HL facility (SLM Solutions GmbH, Germany). The SLM machine is equipped with a

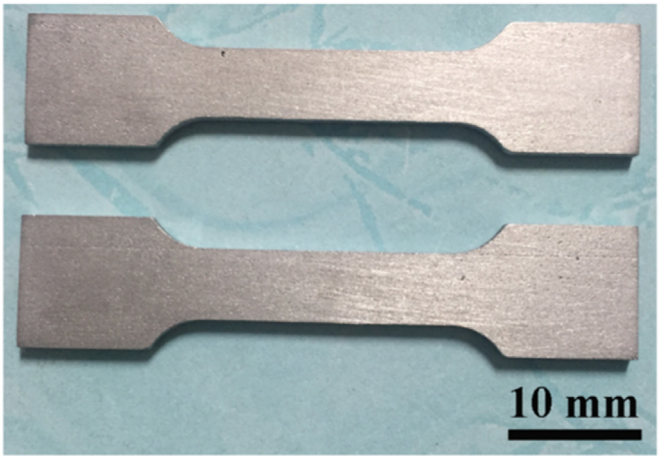

Fig. 1. Tensile specimens of AlSi10Mg alloy made by SLM.

400 W Gaussian beam fiber laser with a focal laser beam diameter ($\Phi_{90\%}$) of 80 μm. The processing parameters have been optimized as follows: the laser power was 350 W, laser scan speed was 1140 mm/s, the powder layer thickness was 50 μm and the scan spacing was 170 μm. The SLM production was performed in an inert argon atmosphere to avoid the pick-up of interstitial oxygen (lower than 0.2%). The AlSi10Mg parts were cut from the Al substrate using wire electrical discharge machining after production. It is worth noting that the substrate was heated to 100 °C for the purpose of reducing internal stress during the SLM process.

2.2. Heat treatment of SLM-produced AlSi10Mg specimens

In accordance with the standard T^6 heat treatment process, the SLM-produced AlSi10Mg specimens were solution-treated at the different temperatures of 450 °C, 500 °C and 550 °C for 2 h, followed by water quenching. After the solution heat treatment, one half of the specimens were immediately subjected to artificial aging at 180 °C for 12 h, and then all the samples were equally water quenched to room temperature [22–27].

2.3. Microstructure and mechanical properties characterization

The microstructure of the as-built and heat-treated SLM AlSi10Mg specimens were characterized using a field emission scanning electron microscope (SEM, JSM-7600F, JEOL, Japan) with an acceleration voltage 15 kV and working distance 8 mm. Before microstructure characterization, the specimens were grounded and polished with an automatic polishing machine (Ecomet300/Automet300, Buehler, America). Keller reagent (vol. 2.5% HNO_3, vol. 1% HF, vol. 1.5% HCl, vol. 95% H_2O) was used to reveal the general structure of the polished sample. X-ray diffraction (XRD) measurements were performed on a XRD-7000S (Shimadzu, Japan) with a Cu tube at 40 kV and 30 mA. The diffraction angle of 2θ varied from 20° to 110° with a step size of 0.02°.

The tensile strength of the AlSi10Mg specimens before and after the heat treatments were characterized by a high-precision electronic universal testing machine (AG-100kN, Shimadzu, Japan) with a constant strain rate of 1 mm/min. The tensile specimen is illustrated in Fig. 1. Vickers hardness tests were carried out on a 430SVD hardness test machine (Wilson Hardness, America) at a load of 1000 gf and a loading time of 15 s. Before mechanical properties testing, all of the test specimens were polished with a 2000 # sand paper to remove the surface layer (e.g. oxidations, contaminations), which would impose a negative influence on the mechanical properties.

3. Results

3.1. XRD analysis

The Al-Si binary phase diagram is implicated in Fig. 2(a). The XRD results of the as-built and heat-treated SLM specimens are shown Fig. 2(b). Based on the Al-Si binary phase diagram, the solidification pathway of the SLM-processed AlSi10Mg has experienced a crystallization reaction $L \rightarrow L + \alpha$ and a eutectic reaction $L \rightarrow \alpha + Si$. The diffraction peaks belong to Al, Si and Mg_2Si according to the JCPDS patterns of 89-2837, 89-5012 and 01-1192 respectively. In the XRD patterns, the Si peaks of the heat-treated specimens have higher intensities than those of the as-built specimens. This indicates a significant decrease of the Si solid solubility in Al matrix after the heat treatments [28]. The solubility of Si in Al matrix was evaluated according to the linear relationship of Vegard's law illustrated in Eq. (1) [28–30], and the lattice parameter of the Al matrix was measured using the shifts in the XRD spectra.

$$a = -0.0032X_{si} + 0.40494 \quad (1)$$

where α is the lattice parameter of the Al matrix, and X_{Si} is the atomic fraction of Si in Al matrix. Based on the Vegard's law, the solubility of Si in Al matrix was found to be 8.89 at% for the as-built SLM specimen. The solubilities of Si in Al matrix for the specimens heat-treated at 450 °C, 500 °C, and 550 °C were calculated to be 3.25, 2.75 and 2.13 at%, respectively. It is worth noting that after artificial aging at 180 °C for 12 h, the intensity of the Si peaks further enhanced. According to Eq. (1), the residual Si in Al matrix were found to be 2.52, 2.02 and 1.68 at% respectively, for the specimens subjected to both solution heat treatment and artificial aging at 180 °C for 12 h, thus indicating that a smaller proportion of Si atoms is further precipitated out from the Al matrix as a result of artificial aging. Moreover, the Mg_2Si XRD peak intensity of the as-built SLM sample is lower than that of the heat-treated samples. This is mainly attributed to the fact that Si precipitates out from the Al matrix after heat treatment, and then the separated Si reacts with Mg to form the Mg_2Si phase [31]. However, the Mg_2Si peaks of the artificial aging samples basically remain unchanged compared to the solution heat-treated samples. This is probably due to the low content of Mg (0.4–0.5 wt%) in AlSi10Mg alloy. Although the artificial aging samples precipitate more Si, there is no residual Mg left to form more Mg_2Si phase, indicating that Mg was limited reactant for generating the Mg_2Si phase [32].

3.2. Microstructure characterization

Fig. 3 depicts the SEM micrographs of the microstructure of the as-built and heat-treated SLM AlSi10Mg samples. A general observation of a single melt track along the scanning direction (x axis) is shown in Fig. 3(a). Unlike the microstructure of AlSi10Mg alloy castings where large rod-like or needle-like Si particles sediment in the Al matrix [5], a novel eutectic microstructure with very fine Si particles has formed. It can be observed that the melt track is characterized with cellular-dendritic microstructure with an average size about 1 μm [33–35]. The grey cellular features are primary α-Al matrix decorated with white fibrous Si network. The fine dispersion of fibrous Si networks in the Al matrix has a positive effect on the mechanical properties of the as-built SLM AlSi10Mg samples. Across the melt track, three distinctive regions with different cellular microstructure in size can be distinguished, namely, coarse cellular zone (C zone), transitional zone (T zone) and fine cellular zone (F zone). These three regions have experienced different thermal histories [5]. The C and T zones corresponding to the boundary of melt track have an average width of about 6 μm and 3 μm, as shown inside the red solid lines and red dashed lines, respectively. For further observation and investigation of the three distinctive regions, high magnification SEM images are shown in Fig.2(b) and (c). It is found that the boundary of melt track is characterized by the relatively coarser cellular microstructure. The cellular sizes in the C zone and T zone were measured to be 2–4 μm and 1–2 μm respectively, whereas the interior of melt pool exhibits the much finer cellular microstructure with an average cell size of 0.6–0.8 μm. Meanwhile, it is remarkable that the eutectic Al-Si network structure is broken to a certain extent by coarsening of the Si into idiomorphic particles in the T zone, which was caused by the increase in diffusion rate of the Si [34].

The effect of solution heat treatment on the microstructure is shown in Fig. 3(d), (e) and (f). The microstructure becomes coarser with increasing the solution temperature from 450 °C to 550 °C. After the artificial aging at 180 °C for 12 h, the microstructure is further coarsened as illustrated in Fig. 3(g), (h) and (i). To investigate the change in size and quantity of the eutectic Si particles upon heat treatment, detailed image analysis was conducted on SEM micrographs obtained from the different heat treatment conditions in Fig. 3. The results, summarized in Fig. 4, illustrate that when the SLM-built AlSi10Mg is solution heat-treated at 450 °C for 2 h, most of the Si particles are less than 1 μm and uniformly dispersed in the Al matrix. With the increase of solution temperature from 500 °C to 550 °C, some of the Si particles have

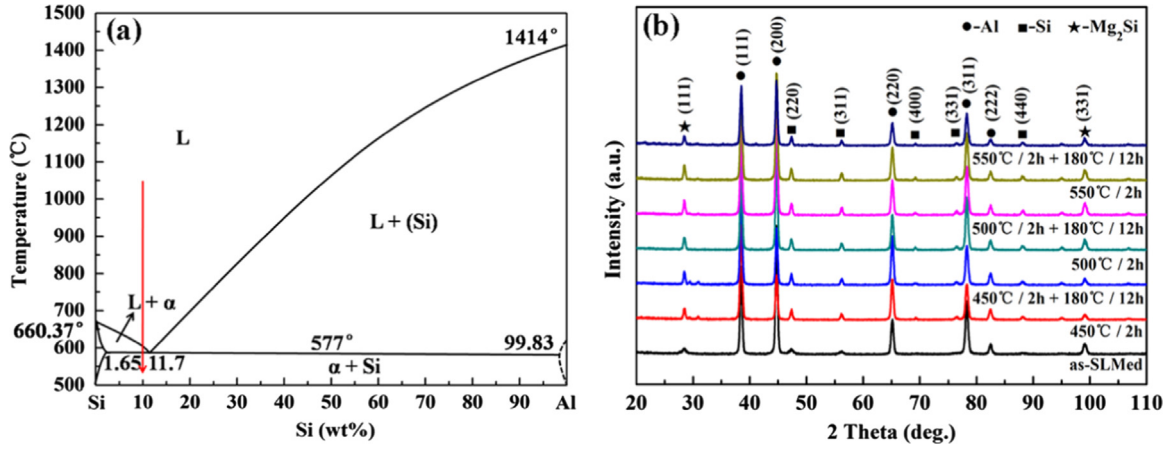

Fig. 2. (a) Al-Si binary phase diagram. Red arrow shows the solidification path and phase transition of Al-10Si. (b) X-ray diffraction patterns of the SLM AlSi10Mg samples processed at different heat treatment conditions.

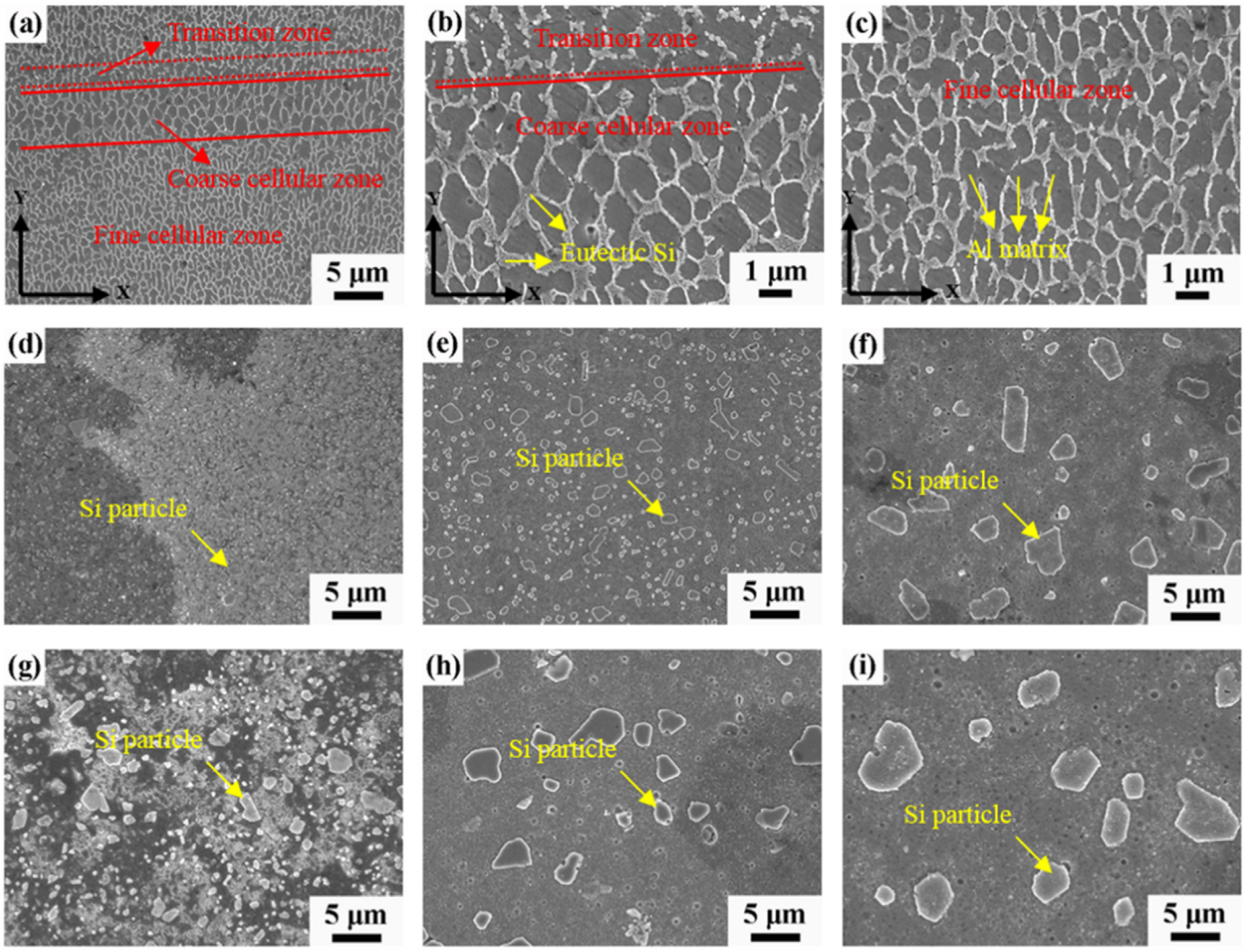

Fig. 3. Micrographs of the as-built and heat-treated SLM AlSi10Mg specimen microstructures after etching with Keller's reagent: (a) single melt track with three distinctive regions; (b) boundary of melt track with coarse cellular region and transition region; (c) interior of melt pool with fine cellular microstructure. SEM images of the eutectic microstructures of the SLM-built AlSi10Mg after different heat treatment conditions: (d) 450 °C for 2 h; (e) 500 °C for 2 h; (f) 550 °C for 2 h; (g) 450 °C for 2 h + 180 °C for 12 h; (h) 500 °C for 2 h + 180 °C for 12 h; and (i) 550 °C for 2 h + 180 °C for 12 h. X-axis is the laser scanning direction and the light grey areas are Si particles.

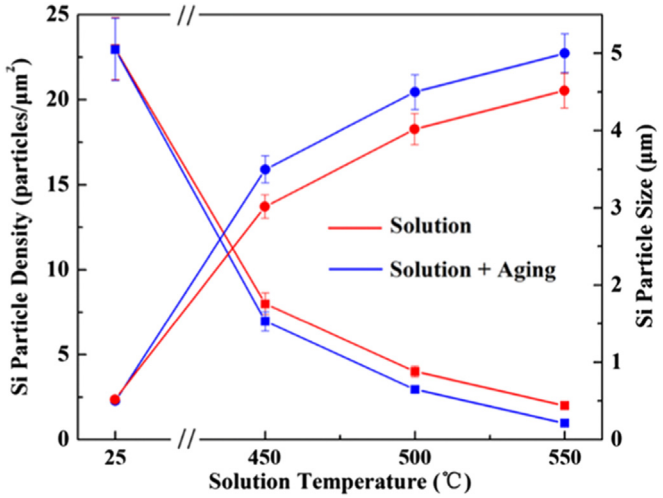

Fig. 4. The Si particle density and size as a function of solution and artificial aging temperature based on the analysis of the SEM images shown in Fig. 3.

been coarsened with the diameter increased from 2 to 4 μm, as illustrated in Fig. 3(e) and (f). Moreover, it is obvious that the Si particles further grow to a size up to 5 μm after the artificial aging, as shown in Fig. 3(g)–(i) and Fig. 4. The increase in the size of Si particles indicates that in the as-built SLM sample, the Al matrix is supersaturated and during the heat treatment the excess Si precipitates out. During the heat treatment, the number of Si particles decreases with increasing the solution temperature, as shown in Fig. 4. The decrease in the number of particles may be attributed to particle coalescence, as well as Ostwald ripening where the large particles grow up at the expense of the small ones [5,36]. The uniform distribution of the Si particles in the microstructure of the as-built specimen is likely due to the precipitation of Si phase along the Al-Si cellular boundaries [37].

It is possible to schematically describe the microstructure evolution of the SLM-produced AlSi10Mg specimens during heat treatment, as shown in Fig. 5. As discussed above, the as-built SLM specimen displays a microstructure consisting of supersaturated Al matrix decorated with fibrous eutectic Si particles (red arrows in Fig. 5) denoted by phase A. After the solution heat treatment and artificial aging, eutectic Si is rejected from the supersaturated Al to form small Si particles denoted by phase B. At this stage, the cellular boundaries become blurred. With the increase in the solution

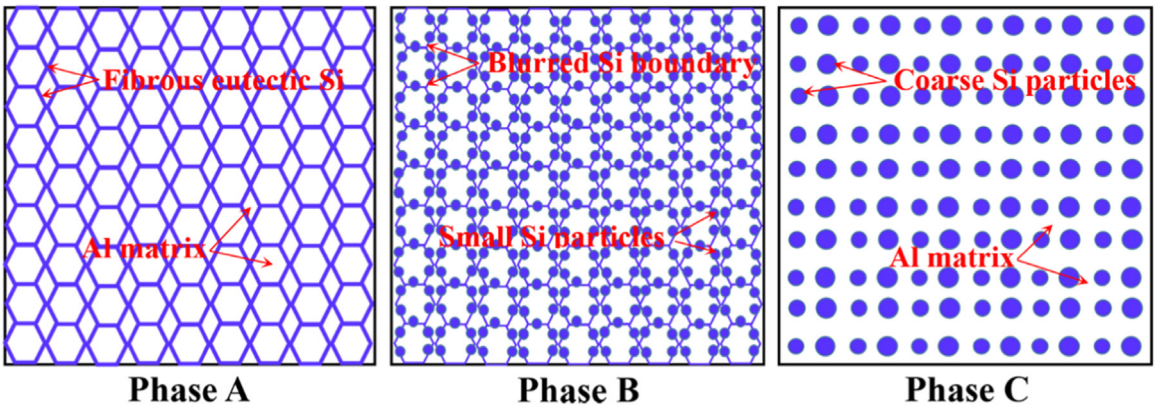

Fig. 5. Schematic of the microstructure evolution of the SLM-produced AlSi10Mg samples during the solution and artificial aging heat treatment. Blue features represent Si-rich areas, while white features represent Al-rich areas. (For interpretation of the references to color in this figure legend, the reader is referred to the web version of this article.)

temperature, the Si particles generally precipitate along the Al-Si cellular boundaries and grow up with their number decreased significantly. Then, the coarse Si particles are evenly distributed on the surface of the Al matrix, which was denoted by phase C.

With the aim of examining the Al, Si and Mg distribution in the SLM-processed specimens after heat treatment in a more detailed way, energy-dispersive X-ray spectroscopy (EDX) analysis was conducted. The SEM image and its corresponding EDX maps of Al, Si and Mg are shown in Fig. 6(a)–(d), respectively. Al mainly fills the matrix (Fig. 6(b)), whereas the Si particles are located in the Al matrix (Fig. 6(c)). From Fig. 6(d), it can be seen that Mg is more evenly distributed compared with Si. But the Mg content on the Si particles is higher than that in the Al matrix. This may be because Mg can react with Si to form Mg_2Si phase, which is associated with a strengthening mechanism in Al-Si-Mg cast alloys.

3.3. Mechanical properties

The tensile stress-strain curves obtained from the room temperature tensile testing on the as-built and different solution heat-treated AlSi10Mg specimens are shown in Fig. 7(a). The variations of the tensile strength, yield strength and ductility with the solution temperature are given in Fig. 7(b). The as-built SLM specimen exhibits the highest tensile and yield strengths of 434.25 ± 10.7 MPa and 322.17 ± 8.1 MPa, respectively, but possesses a lowest ductility of $5.3 \pm 0.22\%$. The solution heat treatment has a great influence on the mechanical properties of the SLM-made AlSi10Mg specimens. As the sample is solution heat-treated at 450 °C for 2 h, there is a dramatically decrease in both tensile and yield strengths (282.36 ± 6.1 MPa and 196.58 ± 3.6 MPa, respectively), whist a large increase in ductility of $13.4 \pm 0.51\%$ can be observed. With further increase of the

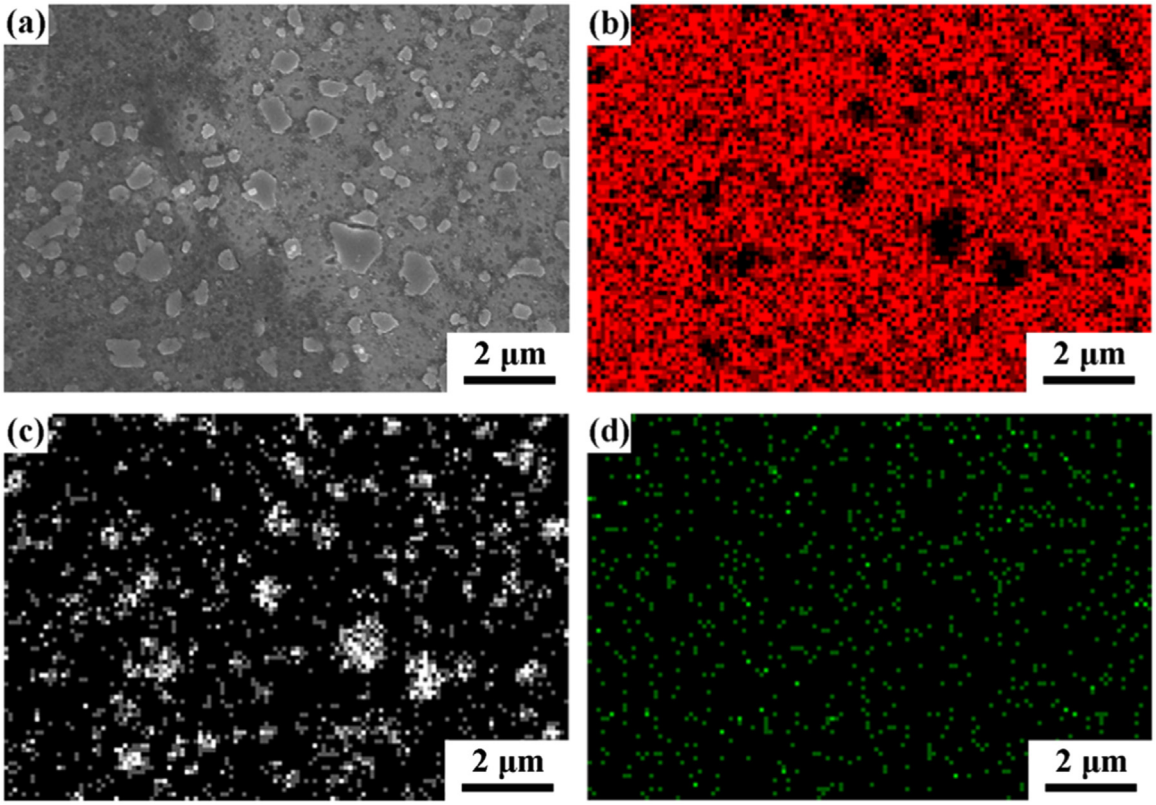

Fig. 6. EDX analysis on the microstructure of the AlSi10Mg solution heat-treated at 500 °C for 2 h. (a) SEM image and corresponding EDX maps of (b) Al; (c) Si; and (d) Mg.

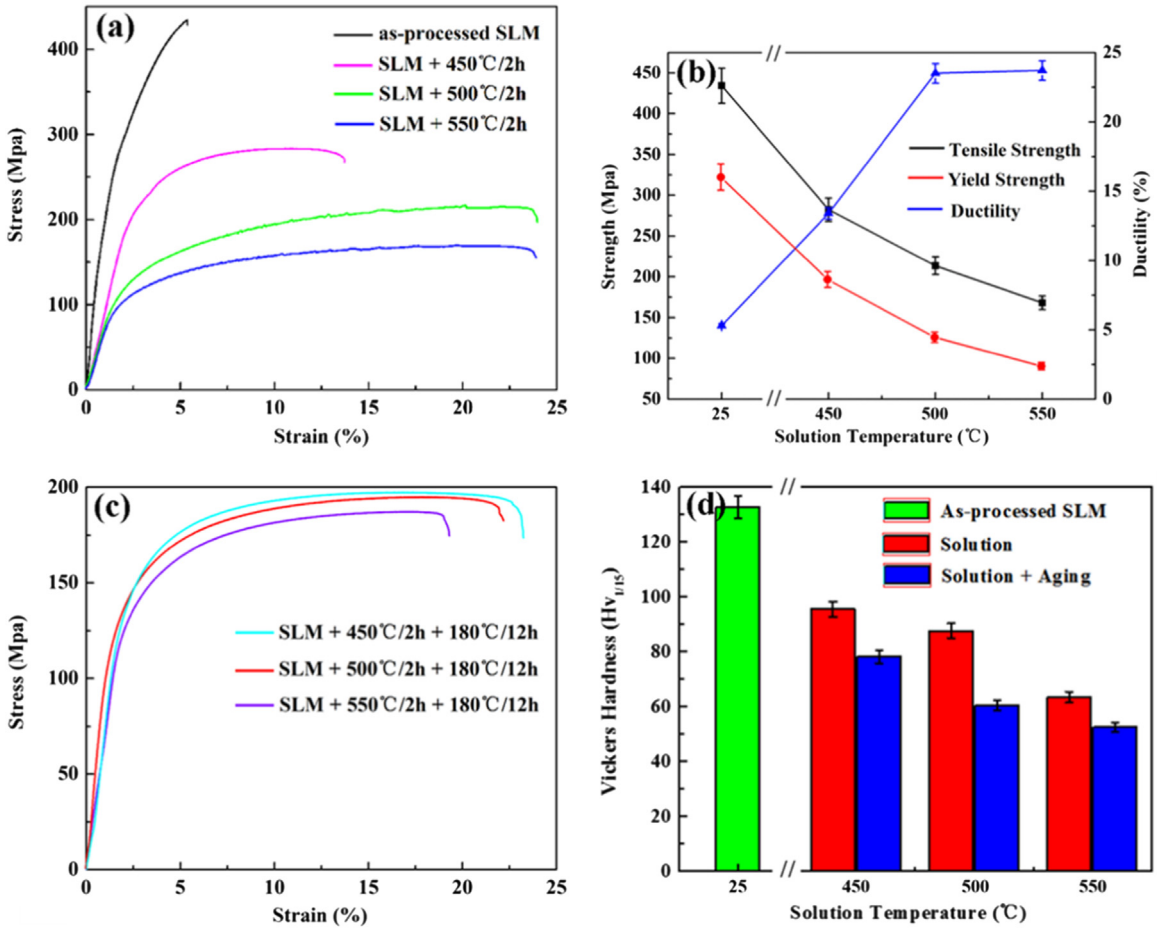

Fig. 7. (a) Room temperature tensile stress-strain curves of the as-built SLM samples that solution heat-treated at different temperatures; (b) corresponding mechanical data; (c) tensile test stress-strain curves of the solution+artificial aging specimens; (d) the Vickers hardness of the as-built and heat-treated SLM specimens.

solution temperature up to 500 °C, the tensile and yield strengths are reduced to 213.75 ± 4.6 MPa and 126.00 ± 2.1 MPa respectively, and the ductility increases to 23.5 ± 0.81%. However, when the solution temperature reaches 550 °C, the specimens exhibit the lowest tensile and yield strengths (168.11 ± 2.4 MPa and 90.52 ± 1.6 MPa, respectively), while the ductility slightly increases to the maximum (23.7 ± 0.84%). For the specimens subjected to both solution heat treatment and artificial aging at 180 °C for 12 h, the mechanical properties are shown in Fig. 7(c). it can be found that the ultimate strength and ductility both decrease with the increase in the solution temperature. The tensile strength decreases from 197.11 ± 3.5 MPa to 187.14 ± 3.1 MPa, while the ductility decreases from 23.3 ± 0.87% to 19.5 ± 0.69%, as the solution temperature increased from 500 °C to 550 °C.

The high strength of the as-built SLM AlSi10Mg specimens can be attributed to the grain refinement. The effect of grain size on the mechanical properties can be rationalized by the semi-empirical Hall-Petch (HP) relationship [38–40], which is indicated in Eq.(2):

$$\sigma = \sigma_0 + kd^{-(1/2)} \tag{2}$$

where σ is the proof stress, σ_0 is the friction stress for dislocation movement, k is the Hall–Petch coefficient, and d is the grain size. The size-induced strengthening results from the pile-up of dislocations at grain boundaries as well as resistance of the dislocations to slip transfer. Grain size refinement leads to reduction of the distance between the Si particles, which can give a considerable contribution to the strength because the increased Al-Si interface can effectively reduce the movement of dislocations. Moreover, due to the nano-sized eutectic network Si in the as-built AlSi10Mg sample, the localized shear stress can be relieved and hence increase the strength. The strength and ductility after heat treatment are influenced by many factors, such as number, morphology and size of the Si phases, initial hardening rate and recovery rate [41]. The last two factors are closely related to the solute content in the solid solution. Upon solution and artificial aging, the Si atoms trapped in the Al matrix are rapidly precipitated out onto the existing eutectic network Si, thus reducing the solid solution strengthening. Meanwhile, the distance between the Si particles increases significantly, which also contributes to the decreased of tensile and yield strengths. As to the ductility of the as-built SLM samples and solution heat-treated specimens in this study, two aspects need to be considered. Firstly, the decrease in the number of Si particles and increase in size induce the reduction of localized stress or strain [5]. Secondly, solution heat treatment reduces the residual stresses that are built up during the SLM process. These two aspects benefit the enhancement of the ductility of the solution heat-treated AlSi10Mg specimens. However, due to the over aging effect, the ductility decreases after the artificial aging.

Hardness is also an important indicator for the material's capability to resist plastic deformation [42–44]. In order to evaluate the influence of heat treatment on the hardness of the as-built SLM AlSi10Mg specimens, Vickers micro-hardness is introduced and the corresponding results are illustrated in Fig. 7(d). In general, the hardness values of the heat-treated specimens are lower than the those of the as-built ones. Due to the fine dispersion of

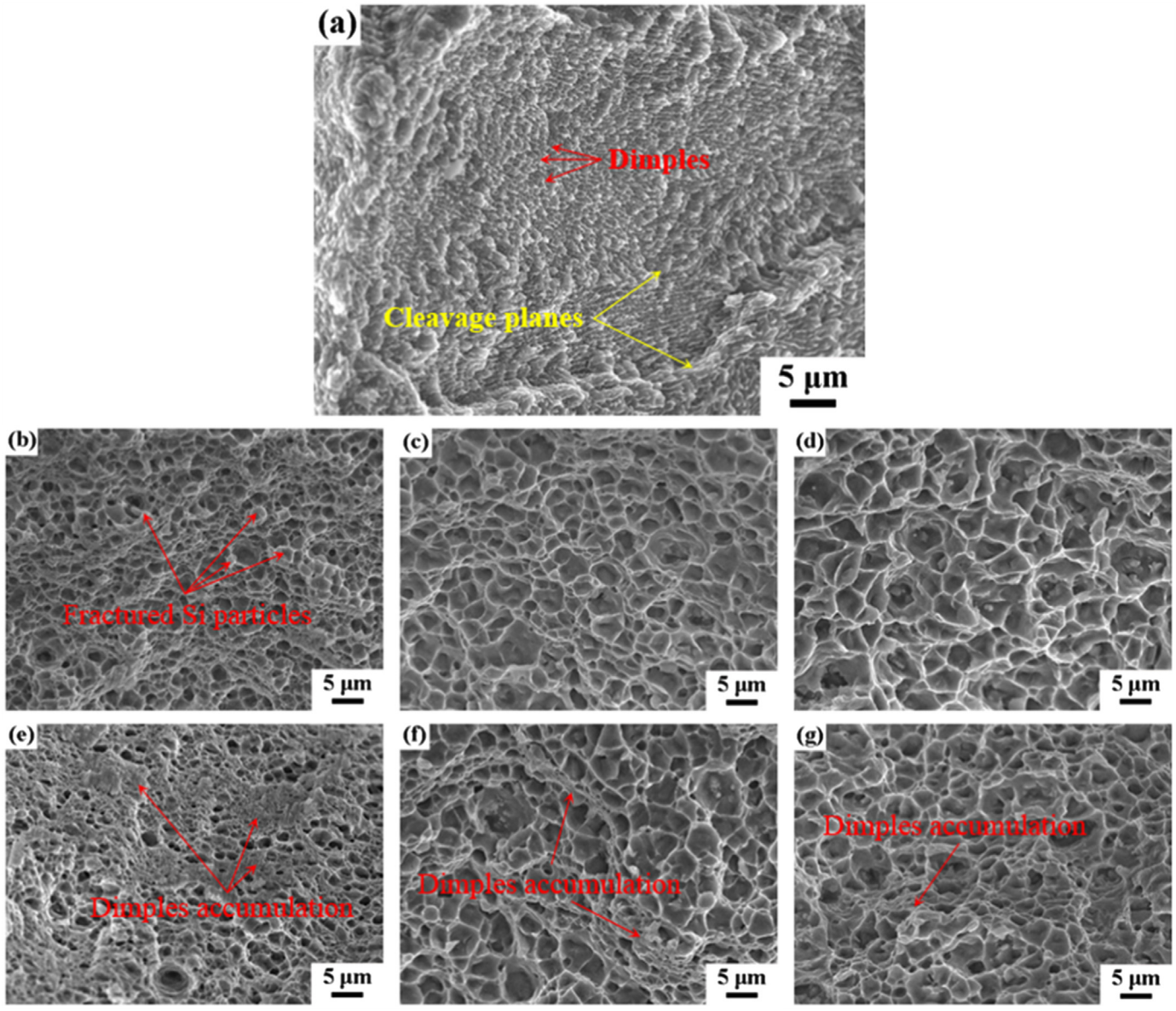

Fig. 8. SEM images of the fracture surfaces of the SLM AlSi10Mg parts with the different heat treatment conditions (a) as-built; (b) 450 °C for 2 h; (c) 500 °C for 2 h; (d) 550 °C for 2 h; (e) 450 °C for 2 h+180 °C for 12 h; (f) 500 °C for 2 h+180 °C for 12 h; and (g) 550 °C for 2 h+180 °C for 12 h, respectively.

eutectic Si in the Al matrix, the as-built AlSi10Mg SLM specimens have the maximum micro-hardness value, namely 132.55 ± 5.3 Hv_1. After the solution treatment at 450 °C for 2 h, a significant decrease in micro-hardness can be observed (95.65 ± 3.6 Hv_1). When the solution treatment temperature is further increased from 500 °C to 550 °C, the micro-hardness decreases from approximately 87.85 ± 3.1 Hv_1 to 63.55 ± 1.9 Hv_1. It is worth noting that artificial aging also has a negative effect on the micro-hardness of the samples that have been subjected to the solution treatment. After the artificial aging at 180 °C for 12 h, the micro-hardness further reduces to 78.15 ± 2.8 Hv_1, 60.55 ± 1.7 Hv_1 and 52.5 ± 1.4 Hv_1 for the specimens that have been solution heat-treated at 450 °C, 500 °C and 550 °C, respectively, as illustrated in the red bars in Fig. 7(d). This behavior is in a good agreement with the evidence found in the tensile tests. This result can be also attributed to the coalescence of small Si particles as well as Ostwald ripening [45], which result in an increase in size and decrease in the number of particles.

3.4. Fracture morphology analysis

Fig. 8 shows the fracture surfaces of the AlSi10Mg samples before and after the heat treatment. The fracture surface of the as-built SLM specimen is illustrated in Fig. 8(a). Apparently, there exist two main morphologies on the fracture surfaces in the forms of dimples and regular stepped cleavage planes [46]. The dimples have a size approximately 1 μm (marked by red arrow in Fig. 8(a)), which are indicative of a ductile fracture. The "river pattern like" stepped cleavage planes (marked by yellow arrow in Fig. 8(a)) show a typical brittle fracture, which is in consistent with the low ductility shown in Fig. 7(a). The fracture features of the as-built SLM AlSi10Mg indicate a ductile as well as a brittle failure. When the sample had been solution heat-treated at 450 °C for 2 h, the equiaxed dimples with an average size around 2 μm are observed across the whole fracture surface, as shown in Fig. 8(b), indicating a highly ductile fracture. Moreover, the fractured Si particles are often observed at the end of the dimples (marked by red arrows in Fig. 8(b)) and no decohesion of the Si particles from the matrix are observed, indicating a good bonding between the Al matrix and Si

particles. As the solution treatment temperature is further increased, the size of the equiaxed dimples increases (Fig. 8(c)–(d)) and reaches 5 μm at 550 °C. A careful observation shows that the edges of the dimples pass through both Al matrix and eutectic Si particles, which further verifies that the eutectic Si is closely connected with the Al matrix. After the artificial aging at 450 °C for 12 h, there is no significant change in the fracture morphologies but a "dimples accumulation" phenomenon (dimples stacked together layer by layer) occurs in the fracture surface (Fig. 8(e)–(g)). Most likely, fracture initiates and propagates through the "dimples accumulation" regions where the plastic deformation capacity is relatively lower [46,47].

4. Discussion

4.1. Unique microstructure of AlSi10Mg processed by SLM

The distinctive features of SLM create a unique microstructure in the as-built AlSi10Mg parts. The characteristics of the microstructure are dependent on the thermal gradient G and the growth rate R [33,34,48]. G is determined by the difference of the temperature over a certain distance and varies with the time and place inside the melt track, R depends on the laser scanning speed and angle between the laser moving direction and the growth direction of the solidifying material. The G over R ratio (G/R) determines the morphology of the microstructure. An equiaxed dendritic, columnar dendritic, cellular and planar are successively expected when the G/R ratio continuously changes from low to high value. The fineness of the microstructure is determined by the cooling rate ($T = G \times R$). The higher cooling rate will lead to greater undercooling, and thus the finer microstructure. SLM is able to generate typical high cooling rate, due to the rapid scanning velocity of the laser beam (1140 mm/s) and high thermal gradient (about 10^5 °C/m) of the processing [34]; therefore, the fine microstructure of the as-built SLM AlSi10Mg sample is achieved. However, because of the Gauss distribution of the laser energy, the undercooling changes over the melt track, which reaches the maximum at the centerline, then gradually decreases along the cross section and finally goes to the minimum at the boundary of the melt track. From this point of view, the cellular size attains the minimum at the center of the melt track, and the maximum value on the boundary of the melt track. For this reason, three different regions, namely coarse cellular zone, transitional zone and fine cellular zone, are present in the microstructure of the as-built SLM specimens.

4.2. Mechanisms for the formation and growth of eutectic Si particles

It is well known that the microstructure of AlSi10Mg alloy can be influenced by superheating [5,49,50]. The underlying reason had been attributed to the existence of two typical temperatures, usually donated by the dissolution temperature T_d and the branching temperature T_b [5,51,52]. At the temperature below T_d, the Al and Si-rich particles which have been inherited from the solid AlSi10Mg alloy exist in the liquid phase. Once the temperature exceeds T_d, these particles begin to be melted. When the temperature is over T_b, molten Al and Si can be considered to mix homogenously [5]. According to previous studies, T_d and T_b of AlSi10Mg alloy should be around 1020 ± 30 °C and 1170 ± 30 °C, respectively [5,51,53], which are much higher than the eutectic temperature of Al-Si alloys (577 °C). During the SLM process, the temperature of a large part of the melt track exceeds T_d but does not reach T_b [5,18]. Hence, a large part of the AlSi10Mg alloy melt track undergoes a superheating condition, which will lead to an inhomogeneous microstructure of the SLM-processed AlSi10Mg alloy. In addition, the short interaction time between laser and material, and the formation of liquid oscillations or capillary waves intensify the inhomogeneous microstructure [53]. Therefore, an inhomogeneous Al-rich and Si-rich microstructure is expected, which is helpful to form heterogeneous nucleation and enhance the nucleation rate. Due to the extremely high cooling rate (about 10^6 °C/s) of SLM [17], the above mentioned inhomogeneous microstructure will retain in the Al matrix [5]. During the solidification process, the Si phase with higher melting point firstly precipitates and grows up in the form of particles most likely by a heterogeneous nucleation mechanism. Then, with the decrease in temperature, the α-*Al* phase then nucleates and grows in the Si depleted zone around the Si particles, which inhibits the growth of the Si particles [54]. The continuous growth of the α-Al phase results in an increased Si concentration in the residual liquid. As the concentration of Si increases to a certain extent, the liquid phase may transform into the eutectic zone eventually [54,55], resulting in the cooperative growth mechanism between Si and Al, and then yielding the eutectic phase in the latter stages of solidification [54,56]. A very steep temperature gradient occurs on the surface of the melted track due to the high laser energy density and heat conductivity of Al [56]. The large temperature gradient induces a highly undercooling condition, leading to the fibrous morphology of the Si crystals [57]. Therefore, a microstructure with fibrous Si network distributed in supersaturated Al matrix forms in the SLM-processed AlSi10Mg alloy.

The fibrous Si phases in the as-built SLM samples are extremely fine (200–300 nm), which results in a large total interfacial energy $\gamma^{Al/Si}$ between Al and Si phases. In addition, other kinetics or thermodynamic factors include the wettability (normally expressed by the contact angle θ_c) and the local concentration of Al and Si atoms. These phenomena provide a high original driving force for the Si atoms coarsening. With the increase in heat treatment temperature, the increased original driving force gives rise to the precipitation of a significant amount of Si from the Al matrix. The availability of the precipitated Si may thus provide an additional contribution to the driving force for the growth of the Si particles. Moreover, when heat-treated at a high temperature, Si phase undergoes a thermally activated growth process. This enables the growth of Si phase along with the lowest free energy direction [5].

5. Conclusions

In this study, the effects of the solution and artificial aging heat treatments on the phase, microstructure and mechanical properties of the SLM-produced AlSi10Mg specimens are systematically studied. The main results and findings are as follows.

(1) The solubility of Si atoms in Al matrix is calculated to be 8.89 at% for the as-built specimens. With the increase in the solution temperature, the solubility decreases rapidly. After artificial aging, the solubility of Si atoms in Al matrix further decreases.

(2) Due to the high cooling rate and thermal fluctuation of the SLM process, an ultrafine eutectic microstructure in the as-built AlSi10Mg specimens is formed. The eutectic microstructure is characterized by eutectic Si network comprising of spherical nano-sized particles embedded in the Al matrix, which gives rise to significantly better tensile properties and Vickers micro-hardness.

(3) Upon solution heat treatment, Si atoms precipitate from the supersaturated Al matrix to form small Si particles. With increasing the solution temperature, the size of the Si particles increases, whereas their number decreases. After artificial aging, the Si particles are further coarsened.

(4) The variation in size of Si particles has a significant influence on the mechanical properties of the AlSi10Mg specimens. The

tensile strength decreases from 434.25 ± 10.7 MPa for the as-built specimens to 168.11 ± 2.4 MPa for the specimens that solution heat-treated at 550 °C for 2 h. in contrast, the fracture strain remarkably increases from 5.3 ± 0.22% to 23.7 ± 0.84%.

This study provides an important insight into the refinement of AlSi10Mg alloy without the addition of other elements, and finds that the microstructure and mechanical properties by SLM-processed AlSi10Mg alloy can be tailored by different heat treatment processes. The findings would be a valuable reference to the optimization of the heat treatment process for the purpose of fabricating AlSi10Mg parts by SLM with acceptable microstructure and mechanical properties.

Acknowledgement

This work was supported by the National Natural Science Foundation of China (51375189 and 51375188). The authors would also like to thank the State key Laboratory of Materials Processing and Die & Mould Technology as well as the Analysis and Testing Center of Huazhong University of Science and Technology for the SEM and tensile properties tests.

References

[1] N. Read, W. Wang, K. Essa, M.M. Attallah, Selective laser melting of AlSi10Mg alloy: process optimization and mechanical properties development, Mater. Des. 65 (2015) 417–424.
[2] B. Li, H.W. Wang, J.C. Jie, Z.J. Wei, Effects of yttrium and heat treatment on the microstructure and tensile properties of Al-7.5Si-0.5Mg alloy, Mater. Des. 32 (2011) 1617–1622.
[3] Y.C. Tsai, C.Y. Chou, S.L. Lee, C.K. Lin, J.C. Lin, S.W. Lim, Effect of trace La addition on the microstructures and mechanical properties of A356 (Al-7Si-0.35Mg) aluminum alloys, J. Alloy. Compd. 487 (2009) 157–162.
[4] S.D. McDonald, K. Nogita, A.K. Dahle, Eutectic nucleation in Al–Si alloys, Acta Mater. 52 (2004) 4273–4280.
[5] X.P. Li, X.J. Wang, M. Saunders, A. Suvorova, L.C. Zhang, Y.J. Liu, M.H. Fang, Z. H. Huang, T.B. Sercombe, A selective laser melting and solution heat treatment refined Al-12Si alloy with a controllable ultrafine eutectic microstructure and 25% tensile ductility, Acta Mater. 95 (2015) 74–82.
[6] L. Lu, K. Nogita, A.K. Dahle, Combining Sr and Na additions in hypoeutectic Al-Si foundry alloys, Mater. Sci. Eng. A 399 (2005) 244–253.
[7] F. Wang, Z.L. Liu, D. Qiu, J.A. Taylor, M.A. Easton, M.X. Zhang, Revisiting the role of peritectics in grain refinement of Al alloys, Acta Mater. 61 (2013) 630–730.
[8] K. Nogita, S.D. McDonald, A.K. Dahle, Eutectic modification of Al-Si alloys with rare earth metals, Mater. Trans. 45 (2004) 323–326.
[9] A. Knuutinen, K. Nogita, S.D. McDonald, A.K. Dahle, Porosity formation in aluminium alloy A356 modified with Ba, Ca, Y and Yb, J. Light Met. 1 (2001) 241–249.
[10] R. Trivedi, F. Jin, I.E. Anderson, Dynamical evolution of microstructure in finely atomized droplets of Al-Si alloys, Acta Mater. 51 (2003) 289–300.
[11] E. Karakösea, M. Keskin, Effect of solidification rate on the microstructure and microhardness of a melt-spun Al-8Si-1Sb alloy, J. Alloy. Compd. 479 (2009) 230–236.
[12] Z.W. Chen, Y.M. Lei, H.F. Zhang, Structure and properties of nanostructured A357 alloy produced by melt spinning compared with direct chill ingot, J. Alloy. Compd. 509 (2011) 7473–7477.
[13] S. Zhang, Q.S. Wei, L.Y. Cheng, S. Li, Y.S. Shi, Effects of scan line spacing on pore characteristics and mechanical properties of porous Ti6Al4V implants fabricated by selective laser melting, Mater. Des. 63 (2014) 185–193.
[14] Q.S. Wei, S. Li, C.J. Han, W. Li, L.Y. Cheng, L. Hao, Y.S. Shi, Selective laser melting of stainless-steel/nano-hydroxyapatite composites for medical applications: microstructure, element distribution, crack and mechanical properties, J. Mater. Process. Technol. 222 (2015) 444–453.
[15] S.F. Wen, S. Li, Q.S. Wei, C.Z. Yan, S. Zhang, Y.S. Shi, Effect of molten pool boundaries on the mechanical properties of selective laser melting parts, J. Mater. Process. Technol. 214 (2014) 2660–2667.
[16] P. Fischer, V. Romano, H.P. Weber, N.P. Karapatis, E. Boillat, R. Glardon, Sintering of commercially pure titanium powder with a Nd:YAG laser source, Acta Mater. 51 (2003) 1651–1662.
[17] Y.L. Li, D.D. Gu, Parametric analysis of thermal behavior during selective laser melting additive manufacturing of aluminum alloy powder, Mater. Des. 63 (2014) 856–867.
[18] P.P. Yuan, D.D. Gu, D.H. Dai, Particulate migration behavior and its mechanism during selective laser melting of TiC reinforced Al matrix nanocomposites, Mater. Des. 82 (2015) 46–55.
[19] C. Weingarten, D. Buchbinder, N. Pirch, W. Meiners, K. Wissenbach, R. Poprawe, Formation and reduction of hydrogen porosity during selective laser melting of AlSi10Mg, J. Mater. Process. Technol. 221 (2015) 112–120.
[20] C.L. Qiu, S. Yue, N.J.E. Adkins, M. Ward, H. Hassanin, P.D. Lee, P.J. Withers, M. M. Attallah, Influence of processing conditions on strut structure and compressive properties of cellular lattice structures fabricated by selective laser melting, Mater. Sci. Eng. A 628 (2015) 188–197.
[21] K. Kempen, L. Thijs, J.V. Humbeeck, J.P. Kruth, Processing AlSi10Mg by selective laser melting: parameter optimisation and material characterization, Mater. Sci. Technol. 31 (2015) 917–923.
[22] E. Brandl, U. Heckenberger, V. Holzinger, D. Buchbinder, Additive manufactured AlSi10Mg samples using Selective Laser Melting (SLM): microstructure, high cycle fatigue, and fracture behavior, Mater. Des. 34 (2012) 159–169.
[23] N.T. Aboulkhair, C. Tuck, I. Ashcroft, I. Maskery, N.M. Everitt, On the precipitation hardening of selective laser melted AlSi10Mg., Metall. Mater. Trans. A 46A (2015) 3337–3341.
[24] M. Tiryakioglu, The effect of solution treatment and artificial aging on the work hardening characteristics of a cast Al-7%Si-0.6%Mg alloy, Mater. Sci. Eng. A 427 (2006) 154–159.
[25] M. Tiryakioglu, Si particle size and aspect ratio distributions in an Al-7%Si-0.6% Mg alloy during solution treatment, Mater. Sci. Eng. A 473 (2008) 1–6.
[26] E. Ogris, A. Wahlen, H. Luchinger, P.J. Uggowitzer, On the silicon spheroidization in Al–Si alloys, J. Light Met. 2 (2002) 263–269.
[27] D.L. Zhang, L.H. Zheng, D.H. StJohn, Effect of a short solution treatment time on microstructure and mechanical properties of modified Al-7 wt%Si-0.3 wt%Mg alloy, J. Light Met. 2 (2002) 27–36.
[28] P. Ma, K.G. Prashanth, S. Scudino, Y.D. Jia, H.W. Wang, C.M. Zou, Z.J. Wei, J. Eckert, Influence of annealing on mechanical properties of Al-20Si processed by selective laser melting, Metal 4 (2014) 28–36.
[29] A. Bendijk, R. Delhez, L. Katgerman, T.H. Dekeijser, E.J. Mittemeijer, N. M. Vanderpers., Characterization of Al-Si-alloys rapidly quenched from the melt, J. Mater. Sci. 15 (1980) 2803–2810.
[30] J. Milligan, R. Vintila, M. Brochu., Nanocrystalline eutectic Al–Si alloy produced by cryomilling, Mater. Sci. Eng. A 508 (2009) 43–49.
[31] X. Xie, J. Shen, L. Cheng, Y. Li, Y.Y. Pu, Effects of nano-particles strengthening activating flux on the microstructures and mechanical properties of TIG welded AZ31 magnesium alloy joints, Mater. Des. 81 (2015) 31–38.
[32] X.L. Izcaraa, A.G. Blanka, F. Pyczak, P. Staron, S. Schumann, N. Huber, Characterization and modeling of the influence of artificial aging on the microstructural evolution of age-hardenable AlSi10Mg (Cu) aluminum alloys, Mater. Sci. Eng. A 610 (2014) 46–53.
[33] C.Z. Yan, L. Hao, A. Hussein, P. Young, J.T. Huang, W. Zhu, Microstructure and mechanical properties of aluminium alloy cellular lattice structures manufactured by direct metal laser sintering, Mater. Sci. Eng. A 628 (2015) 238–246.
[34] L. Thijs, K. Kempen, J.P. Kruth, J.V. Humbeeck, Fine-structured aluminium products with controllable texture by selective laser melting of pre-alloyed AlSi10Mg powder, Acta Mater. 61 (2013) 1809–1819.
[35] E. Louvis, P. Fox, C.J. Sutcliffe, Selective laser melting of aluminium components, J. Mater. Process. Technol. 211 (2011) 275–284.
[36] M.E. Glicksman, Principles of Solidification, Springer, NewYork, 2011.
[37] K.G. Prashanth, S. Scudino, H.J. Klauss, K.B. Surredd, L. Löber, Z. Wang, A. K. Chaubey, U. Kühn, J. Eckert, Microstructure and mechanical properties of Al-12Si produced by selective laser melting: effect of heat treatment, Mater. Sci. Eng. A 590 (2014) 153–160.
[38] M.R. Basariya, V.C. Srivastava, N.K. Mukhopadhyay, Microstructural characteristics and mechanical properties of carbon nanotube reinforced aluminum alloy composites produced by ball milling, Mater. Des. 64 (2014) 542–549.
[39] X.H. Dong, X.T. Hong, F. Chen, B.R. Sang, W. Yu, X.P. Zhang, Effects of specimen and grain sizes on compression strength of annealed wrought copper alloy at room temperature, Mater. Des. 64 (2014) 400–406.
[40] Y.Z. Zhu, S.Z. Wang, B.L. Li, Z.M. Yin, Q. Wan, P. Liu, Grain growth and microstructure evolution based mechanical property predicted by a modified Hall–Petch equation in hot worked Ni76Cr19AlTiCo alloy, Mater. Des. 55 (2014) 456–462.
[41] Y. Chen, M. Weyland, C.R. Hutchinson, The effect of interrupted aging on the yield strength and uniform elongation of precipitation-hardened Al alloys, Acta Mater. 61 (2013) 5877–5894.
[42] D. Buchbinder, H. Schleifenbaum, S. Heidrich, W. Meiners, J. Bültmann., High power selective laser melting (HP SLM) of aluminum parts, Phys. Procedia 12 (2011) 271–278.
[43] J.M. Mendoza-Duarte, I. Estrada-Guel, C. Carreño-Gallardo, R. Martínez-Sánchez, Study of Al composites prepared by high-energy ball milling; effect of processing conditions, J. Alloy. Compd. 643 (2015) S172–S177.
[44] F. Shehata, A. Fathy, M. Abdelhameed, S.F. Moustafa, Fabrication of copper–alumina nanocomposites by mechano-chemical routes, J. Alloy. Compd. 476 (2009) 300–305.
[45] A.E.W. Jarfors, H. Keife, T. Antonsson, Deformation enhanced liquid phase sintering (DELPS): a study on the use of partial adiabatic melting during powder consolidation, J. Mater. Process. Technol. 127 (2002) 159–164.
[46] D. Hull, Observing Measuring and Interpreting Fracture Surface Topography, Cambridge University Press, Cambridge, 1999.
[47] S. Hegde, K.N. Prabhu, Modification of eutectic silicon in Al-Si alloys, J. Mater. Sci. 43 (2008) 3009–3027.
[48] D. Manfredi, F. Calignano, M. Krishnan, R. Canali, E. Ambrosio, E. Atzeni, From

powders to dense metal parts: characterization of a commercial AlSiMg alloy processed through direct metal laser sintering, Mater 6 (2013) 856–869.
[49] J. Wang, S.X. He, B.D. Sun, Q.X. Guo, M. Nishio, Grain refinement of Al-Si alloy (A356) by melt thermal treatment, J. Mater. Process. Technol. 141 (2003) 29–34.
[50] S. Nafisi, D. Emadi, M.T. Shehata, R. Ghomashchi, Effects of electromagnetic stirring and superheat on the microstructural characteristics of Al-Si-Fe alloy, Mater. Sci. Eng. A 432 (2006) 71–83.
[51] M. Calvo-Dahlborga, P.S. Popel, M.J. Kramer, M. Besser, J.R. Morris, U. Dahlborg, Superheat-dependent microstructure of molten Al–Si alloys of different compositions studied by small angle neutron scattering, J. Alloy. Compd. 550 (2013) 9–24.
[52] I.G. Brodova, P.S. Popel, G.I. Eskin, Liquid Metal Processing: Application to Aluminium Alloy Production, Taylor & Francis, London, 2002.
[53] W.D. Liu, L.M. Ye, K.X. Liu, Micro-nano scale ripples on metallic glass induced by laser pulse, J. Appl. Phys. 109 (2011) 043109-1-5.
[54] M.C. Flemings, Solidification Processing, McGraw-Hill, New York, NY, USA, 1974.
[55] M. Gremaud, D.R. Allen, M. Rappaz, J.H. Perepezko, The development of nucleation controlled microstructures during laser treatment of Al-Si alloys, Acta Mater. 44 (1996) 2669–2681.
[56] Y.T. Pei, J. De Hossen, M. Th., Functionally graded materials produced by laser cladding, Acta Mater. 48 (2000) 2617–2624.
[57] J.W. Yeh, S.Y. Yuan, C.H. Peng, A reciprocating extrusion process for producing hypereutectic Al-20 wt% Si wrought alloys, Mater. Sci. Eng. A 252 (1998) 212–221.